Exploring Spin-tidal field correlations of Dark Matter haloes

Sumit Kumar Adhya

Guide: Prof. Shadab Alam

January 11, 2026

Contents

Brief Review of Tidal Torque Theory

We review linear tidal torque theory here following [2]. Before we start off, let's recall our knowledge of Lagrangian and Eulerian co-ordinates/frames from fluid dynamics.

- Lagrangian co-ordinates: The observer follows an individual particle labelled by $'\mathbf{q}'$, which is the lagrangian coordinate of the particle, as it moves through space and time. These labels are given to all the particles in the system by some time independent vector field $'\mathbf{q}'$. Often $'\mathbf{q}'$ is chosen to be the co-ordinates of the particles (COM, in case of parcels of particles) at some initial time. The flow of the particles is given by some function $\mathbf{X}(\mathbf{q}, t)$ giving the position of particle (or parcel) labelled $'\mathbf{q}'$ at time t.

- Eulerian co-ordinates: This is the laboratory frame observing the system of particles with a fixed grid. Properties like velocities, pressure, temperature are then observed at specific points in this grid. Particles pass through the grid and their velocities are given by a velocity field $\mathbf{u}(\mathbf{x}, t)$, which gives the velocity of some particle at point $\mathbf{x}$ and time t.

In the Lagrangian frame, we focus on an individual particle and in Eulerian frame, we focus on an individual point. The two specifications can be related as:

$$\mathbf{u}(\mathbf{X}(\mathbf{q}, t)) = \frac{\partial \mathbf{X}(\mathbf{q}, t)}{\partial t} \tag{1.1}$$

Suppose we have a flow field $\mathbf{u}(\mathbf{x}, t)$ and a generic field with eulerian specification $F(\mathbf{x}, t)$. Now the rate of change of F experienced by a specific flow particle/parcel would be given by:

$$\frac{DF}{Dt} = \frac{\partial F}{\partial t} + (\mathbf{u} \cdot \nabla) F \tag{1.2}$$

where $DF/Dt = \partial F(\mathbf{X}(\mathbf{q}, t), t)/\partial t$ goes by the names Material derivative, Lagrangian derivative, convective derivative, substantial derivative, or particle derivative.

Now let's proceed towards summarising the basics of linear tidal torque theory. The angular momentum of a proto-halo occupying an Eulerian volume γ that is destined to end up in a virialized halo is:

$$\mathbf{L}(t) = \int_\gamma \rho(\mathbf{r}, t)[\mathbf{r}(t) - \mathbf{r}_{\mathrm{cm}}(t)] \times [\mathbf{v}(t) - \mathbf{v}_{\mathrm{cm}}(t)] d^3 r \tag{1.3}$$

In comoving units:

$$\mathbf{L}(t) = \bar{\rho}(t) a^5(t) \int_\gamma [1 + \delta(\mathbf{x}, t)][\mathbf{x}(t) - \mathbf{x}_{\mathrm{cm}}(t)] \times \dot{\mathbf{x}} d^3 x \tag{1.4}$$

where $\delta(\mathbf{x}, t) = \rho(\mathbf{x}, t)/\bar{\rho}(t) - 1$ is the density contrast. In the matter dominated era, $\bar{\rho}(t) a^3(t) = \bar{\rho}_0 a_0^3$, where the subscript 0 denotes present time. In the Lagrangian description:

$$\mathbf{x}(\mathbf{q}, t) = \mathbf{q} + \mathbf{S}(\mathbf{q}, t) \tag{1.5}$$

Assuming small fluctuations or a smoothed flow, the mapping $\mathbf{q} \to \mathbf{x}$ is reversible. This is because there would be a one to one correspondence between $\mathbf{q}$ and $\mathbf{x}$, in other words as long as the flow remains "smooth" and particles have not yet collided or crossed paths, every initial position $\mathbf{q}$ corresponds to exactly one current position $\mathbf{x}$, implying a laminar flow where the Jacobian determinant $J = ||\partial \mathbf{x}/\partial \mathbf{q}||$ is non-vanishing. We can derive the relation between density and the Jacobian through the conservation of mass. The mass within a fluid element

remains constant, $\rho(\mathbf{x}, t)d^3x = \bar{\rho}(t)d^3q$. Using the volume transformation $d^3x = Jd^3q$, we obtain $\rho J = \bar{\rho}$. Recalling that $1 + \delta = \rho/\bar{\rho}$, this yields:

$$1 + \delta(\mathbf{x}, t) = J^{-1}(\mathbf{q}, t) \tag{1.6}$$

Substituting this into our expression for $\mathbf{L}(t)$, the $(1+\delta)$ term cancels strictly with the Jacobian factor from the volume element transformation $d^3x = Jd^3q$. The integration domain transforms from the Eulerian volume γ to the Lagrangian region Γ. Noting that $\dot{\mathbf{x}} = \dot{\mathbf{S}}$ and $\mathbf{x} - \mathbf{x}_{\mathrm{cm}} = (\mathbf{q} - \bar{\mathbf{q}}) + (\mathbf{S} - \bar{\mathbf{S}})$, we obtain:

$$\mathbf{L}(t) = a^2(t)\bar{\rho}_0 a_0^3 \int_\Gamma [\mathbf{q} - \bar{\mathbf{q}} + \mathbf{S}(\mathbf{q}, t) - \bar{\mathbf{S}}] \times \dot{\mathbf{S}}(\mathbf{q}, t)d^3q \tag{1.7}$$

where barred quantities denote averages over Γ in Lagrangian space. This equation is exact in the absence of orbit-crossing. The linearized continuity and Euler equations in comoving coordinates are:

$$\frac{\partial \delta}{\partial t} + \frac{1}{a}\nabla_x \cdot \mathbf{u} = 0 \tag{1.8}$$

$$\frac{\partial \mathbf{u}}{\partial t} + H\mathbf{u} = -\frac{1}{a}\nabla_x \phi \tag{1.9}$$

where $H = \dot{a}/a$ is the Hubble parameter and ϕ is the peculiar gravitational potential, related to the density by the comoving Poisson's equation:

$$\nabla_x^2 \phi = 4\pi G\bar{\rho}a^2\delta \tag{1.10}$$

Taking the divergence of the Euler equation and the time derivative of the continuity equation allows us to decouple the variables. Combining them yields the evolution equation for density perturbations:

$$\frac{\partial^2 \delta}{\partial t^2} + 2H\frac{\partial \delta}{\partial t} - 4\pi G\bar{\rho}\delta = 0 \tag{1.11}$$

The solution is a superposition of a growing mode $D_+(t)$ and a decaying mode $D_-(t)$. We focus on the growing mode, such that $\delta(\mathbf{x}, t) = \delta_0(\mathbf{x})D_+(t)$.

In the Lagrangian description, the position of a fluid element is $\mathbf{x}(\mathbf{q}, t) = \mathbf{q} + \mathbf{S}(\mathbf{q}, t)$. To relate the density contrast to the displacement, we use the conservation of mass, which implies $\rho(\mathbf{x}, t)d^3x = \bar{\rho}d^3q$. In terms of the density contrast δ, this requires $1 + \delta = J^{-1}$, where $J = \det(\partial \mathbf{x}/\partial \mathbf{q})$ is the Jacobian determinant of the mapping. The Jacobian matrix is given by $\partial \mathbf{x}/\partial \mathbf{q} = \mathbf{I} + \partial \mathbf{S}/\partial \mathbf{q}$. For small perturbations where the displacement gradients are small ($|\partial S_i/\partial q_j| \ll 1$), we can approximate the determinant using the identity $\det(\mathbf{I}+\mathbf{A}) \approx 1 + \mathrm{Tr}(\mathbf{A})$. Thus, $J \approx 1 + \nabla_q \cdot \mathbf{S}$. Substituting this into the density relation and performing a first-order Taylor expansion yields:

$$\delta = \frac{1}{J} - 1 \approx \frac{1}{1 + \nabla_q \cdot \mathbf{S}} - 1 \approx (1 - \nabla_q \cdot \mathbf{S}) - 1 = -\nabla_q \cdot \mathbf{S} \tag{1.12}$$

Since δ evolves as $D_+(t)$, the displacement field must separate into temporal and spatial parts: $\mathbf{S}(\mathbf{q}, t) = D_+(t)\mathbf{P}(\mathbf{q})$.

From the Euler equation, the flow is considered irrotational ($\nabla \times \mathbf{u} = 0$) in the linear regime. This is because primordial fluctuations are scalar in nature, and gravity—being a conservative force—cannot generate vorticity in a pressureless fluid before shell-crossing occurs. Consequently, the peculiar velocity $\mathbf{u} = a\dot{\mathbf{S}}$ and the displacement $\mathbf{S}$ must be gradients of a scalar field. We define the time-independent potential $\Phi(\mathbf{q})$ such that:

$$\mathbf{S}(\mathbf{q}, t) = -D_+(t)\nabla_q \Phi(\mathbf{q}) \tag{1.13}$$

It is important to note that $\Phi(\mathbf{q})$ is a scaled velocity potential (or Lagrangian potential). While related to the physical gravitational potential ϕ via Poisson's equation, Φ is re-scaled by $(4\pi G\bar{\rho}a^2 D_+)^{-1}$ to ensure it is time-independent. This separation allows us to treat Φ as a static spatial template representing the initial seeds of structure, while $D_+(t)$ governs the growth amplitude.

Substituting this back into Poisson's equation ($\delta \propto \nabla^2\phi$ and $\delta \propto \nabla \cdot \mathbf{S} \propto -\nabla^2\Phi$) confirms that Φ is the spatial part of the initial gravitational potential.

The angular momentum $\mathbf{L}$ of the Lagrangian volume Γ is:

$$\mathbf{L}(t) = a^5\bar{\rho}\int_\Gamma (\mathbf{x} - \bar{\mathbf{x}}) \times \dot{\mathbf{x}}\,d^3q \tag{1.14}$$

Using $\mathbf{x} = \mathbf{q} + \mathbf{S}$ and $\dot{\mathbf{x}} = \dot{\mathbf{S}}$, and defining relative coordinates $\mathbf{q}' = \mathbf{q} - \bar{\mathbf{q}}$ and $\mathbf{S}' = \mathbf{S} - \bar{\mathbf{S}}$, we expand the cross product:

$$(\mathbf{x} - \bar{\mathbf{x}}) \times \dot{\mathbf{x}} = (\mathbf{q}' + \mathbf{S}') \times \dot{\mathbf{S}}' = \mathbf{q}' \times \dot{\mathbf{S}}' + \mathbf{S}' \times \dot{\mathbf{S}}' \tag{1.15}$$

Under the Zel'dovich approximation, $\mathbf{S}(\mathbf{q}, t)$ and $\dot{\mathbf{S}}(\mathbf{q}, t)$ are parallel vectors because they share the same spatial direction vector $\nabla\Phi(\mathbf{q})$. Specifically, $\mathbf{S}' \times \dot{\mathbf{S}}' \propto \nabla\Phi \times \nabla\Phi = 0$. This vanishing of the self-term is a direct result of the irrotational assumption. The integral simplifies to:

$$\mathbf{L}(t) = \bar{\rho}_0 a^2(t) \int_\Gamma \mathbf{q}' \times \dot{\mathbf{S}}(\mathbf{q}, t)\,d^3q \tag{1.16}$$

Substitute $\dot{\mathbf{S}} = -\dot{D}_+(t)\nabla\Phi(\mathbf{q})$:

$$\mathbf{L}(t) = -a^2(t)\dot{D}_+(t)\bar{\rho}_0 \int_\Gamma \mathbf{q}' \times \nabla\Phi(\mathbf{q})\,d^3q \tag{1.17}$$

We assume the potential $\Phi(\mathbf{q})$ varies smoothly across the proto-halo and expand it in a Taylor series about the center of mass ($\mathbf{q}' = 0$):

$$\Phi(\mathbf{q}) \approx \Phi(\mathbf{0}) + \left.\frac{\partial\Phi}{\partial q_i}\right|_0 q_i' + \frac{1}{2}\left.\frac{\partial^2\Phi}{\partial q_i \partial q_j}\right|_0 q_i' q_j' \tag{1.18}$$

Taking the gradient $\nabla\Phi$:

$$\frac{\partial\Phi}{\partial q_k} \approx \left.\frac{\partial\Phi}{\partial q_k}\right|_0 + \left.\frac{\partial^2\Phi}{\partial q_k \partial q_l}\right|_0 q_l' \tag{1.19}$$

We substitute this into the integral for the i-th component of angular momentum:

$$L_i(t) \approx -a^2\dot{D}\bar{\rho}_0\epsilon_{ijk}\int_\Gamma q_j'\left(\left.\frac{\partial\Phi}{\partial q_k}\right|_0 + \left.\frac{\partial^2\Phi}{\partial q_k \partial q_l}\right|_0 q_l'\right)d^3q \tag{1.20}$$

The first term vanishes as $\int q_j' d^3q = 0$ at the center of mass. The second term yields:

$$L_i(t) = -a^2(t)\dot{D}(t)\epsilon_{ijk}\left(\left.\frac{\partial^2\Phi}{\partial q_k \partial q_l}\right|_0\right)\left(\bar{\rho}_0\int_\Gamma q_j' q_l' d^3q\right) \tag{1.21}$$

We identify the two physical tensors:

- Deformation (Tidal) Tensor: $\mathcal{D}_{kl} \equiv -\left.\frac{\partial^2\Phi}{\partial q_k \partial q_l}\right|_0$

- Inertia Tensor: $I_{jl} \equiv \bar{\rho}_0 a_0^3 \int_\Gamma q_j' q_l' d^3q$

Substituting these back, we arrive at the final result:

$$L_i(t) = a^2(t)\dot{D}(t)\epsilon_{ijk}\mathcal{D}_{kl}I_{lj} \tag{1.22}$$

This confirms that angular momentum arises from the misalignment between the principal axes of the proto-halo's inertia tensor and the external tidal shear field.

Reproducing Sujatha et. al. 2019

2.1   Introduction

The goal of this section is to reproduce the main result of the paper: Tidal web anisotropy (α) is a primary indicator of halo assembly bias. We use the Sahyadri N body simulation data for our analysis. But before that we recall some key definitions from the paper which would be useful for our analysis.

2.2   Measuring internal halo properties

All internal halo properties used in the analysis are computed using only gravitationally bound particles belonging to the FoF group of each halo. Below we summarise the definitions and notation used.

Mass ellipsoid tensor and shape

The mass ellipsoid (shape) tensor M_{ij} of a halo is computed by summing over bound particles following the iterative prescription of Allgood et. al. (2006):

$$M_{ij} \;=\; \sum_{n \in \text{halo}} \frac{x_{n,i}\,x_{n,j}}{r_n^2}\,, \tag{2.1}$$

where $x_{n,i}$ is the i-th component of the n-th particle position relative to the halo centre and

$$r_n^2 \;=\; x_n^2 \;+\; \frac{y_n^2}{(b/a)^2} \;+\; \frac{z_n^2}{(c/a)^2} \tag{2.2}$$

is the ellipsoidal distance used during iteration. Diagonalising M_{ij} yields ordered eigenvalues $a^2 \geq b^2 \geq c^2$. Common summary measures are:

- the minor-to-major axis ratio, c/a, with $0 \leq c/a \leq 1$; $c/a = 1$ corresponds to a sphere.

- the triaxiality parameter, $T = (a^2 - b^2)/(a^2 - c^2)$, which indicates whether the ellipsoid is prolate ($T \to 1$) or oblate ($T \to 0$).

Velocity ellipsoid tensor

The velocity ellipsoid tensor measures anisotropy in the halo velocity dispersion. For a halo with N particles:

$$V_{ij}^2 \;=\; \frac{1}{N} \sum_{n \in \text{halo}} (v_{n,i} - \langle v_i \rangle)\,(v_{n,j} - \langle v_j \rangle)\,, \tag{2.3}$$

where $v_{n,i}$ is the i-th velocity component of the n-th particle and $\langle v_i \rangle$ is the bulk halo velocity. Diagonalising V_{ij}^2 gives eigenvalues $a_v^2 \geq b_v^2 \geq c_v^2$ and we use the ratio c_v/a_v as a measure of the velocity-ellipsoid asphericity (analogous to c/a for the mass ellipsoid).

Velocity anisotropy

The (global) velocity anisotropy β is defined by

$$\beta = 1 - \frac{\sigma_t^2}{2\sigma_r^2}, \tag{2.4}$$

where σ_r^2 and σ_t^2 are the radial and tangential velocity dispersions of halo particles (computed inside the mass ellipsoid). $\beta = 0$ corresponds to an isotropic velocity distribution; $\beta > 0$ indicates radial dominance, while $\beta < 0$ indicates tangential dominance.

Concentration

Halo concentration c_{vir} is measured by fitting the spherically averaged density profile to an NFW form,

$$\rho(r) = \frac{\rho_s}{(r/r_s)(1 + r/r_s)^2}, \tag{2.5}$$

and defining

$$c_{\mathrm{vir}} \equiv \frac{R_{\mathrm{vir}}}{r_s}, \tag{2.6}$$

where r_s is the NFW scale radius from the fit. Concentration is a commonly used proxy for formation epoch.

Spin

The (Peebles) dimensionless spin parameter λ is

$$\lambda = \frac{J\,|E|^{1/2}}{G\,M_{\mathrm{vir}}^{5/2}}, \tag{2.7}$$

where J is the halo angular momentum magnitude, E its total energy, M_{vir} the virial mass and G Newton's constant. Rockstar also provides the Bullock variant

$$\lambda' = \frac{J_{\mathrm{vir}}}{\sqrt{2}\,M_{\mathrm{vir}}\,R_{\mathrm{vir}}\,V_{\mathrm{vir}}} \tag{2.8}$$

which is sometimes used interchangeably; both quantify rotational support of the halo.

Tidal anisotropy α

Tidal anisotropy quantifies the degree to which the local tidal field around a halo is anisotropic. We follow the same definition used in the reference work and in our pipeline: the tidal tensor is evaluated at a fixed scale ($4 \times R_{200b}$ in our case) and diagonalised to obtain its eigenvalues $\lambda_1, \lambda_2, \lambda_3$ (ordered arbitrarily in the catalog). From these we construct two scalar combinations that capture the isotropic and anisotropic parts of the tidal field used throughout this work:

$$\mathrm{trace} = \delta = \lambda_1 + \lambda_2 + \lambda_3$$

$$q^2 = \tfrac{1}{2}\Big[(\lambda_1 - \lambda_2)^2 + (\lambda_1 - \lambda_3)^2 + (\lambda_2 - \lambda_3)^2\Big]$$

The tidal anisotropy α is then defined as

$$\alpha = \frac{\sqrt{q^2}}{1 + \delta}.$$

This form isolates the anisotropic shear (numerator) and normalises by the local isotropic compression/expansion (denominator), so α is large only when shear is substantial relative to the local density. In our implementation we compute λ_i from the columns `lam1_R4R200b`, `lam2_R4R200b` and `lam3_R4R200b` in the provided catalogue and then compute q^2, δ and α exactly as above.

Halo bias b_1

Halo bias describes how strongly haloes of a given population trace (or are biased relative to) the underlying matter distribution on large scales. In the analyses and plots of this report we use a halo-by-halo estimator of the large-scale linear bias, denoted b_1, provided in the halo catalogue (column `b1`). In the original reference this quantity is obtained by comparing the halo overdensity to the matter overdensity on sufficiently large scales.

Notes on measurement

- All of the above quantities are computed using bound particles assigned by the halo finder (rockstar), and in practice the mass ellipsoid and velocity ellipsoid calculations restrict the particle sums to the relevant ellipsoidal region.

- Iterative procedures are used where needed (mass ellipsoid determination), starting from a spherical guess and updating axis ratios until convergence.

- These scalar summaries (e.g. c/a, c_v/a_v, β, c_{vir}, λ) are the quantities used in the assembly-bias analysis (section 3) and are compared to the tidal-anisotropy α and halo-by-halo bias b_1.

2.3 Sahyadri Simulation data

In our analysis, we use the data from the Sahyadri N-body cosmological simulation at redshift z=0. The dataset contains dark matter halo catalogs generated using the ROCKSTAR halo finder and include comprehensive halo properties across three files-basic, extended and vahc. The Basic catalog contains essential halo properties including masses, radii, positions, velocities, and basic shape parameters. The Extended catalog contains detailed halo properties including merger tree information, accretion history, spin parameters, and shape measurements and the Vahc catalog contains Velocity Anisotropy Halo Catalog (VAHC) data - custom calculations from the Sahyadri simulation measuring tidal tensor eigenvalues at different radial scales. These parameters characterize the local tidal environment around each halo.

The data we have for $z = 0$ contains information for 10549241 haloes. For our study we first convert the fits files into csv's., followed by extracting the relevant columns into a pandas dataframe.

To understand some basic features and trends followed by the haloes, we obtain the following plots.

Inference:-

1. **Halo Mass Function:** The halo mass distribution exhibits a steep decline toward higher masses. The majority of halos occupy the intermediate mass range (10^9–$10^{11}\,M_\odot/h$), while massive cluster-scale halos ($> 10^{12}\,M_\odot/h$) are comparatively rare, as expected from hierarchical assembly. Larger/More massive haloes correspond to, very high overdensities in the primorial field which is rarer and statistically much less likely.

2. **Kinematic Relations (v_{rms} and V_{peak}):** Both the velocity dispersion (v_{rms}) and the peak circular velocity (V_{peak}) scale positively with halo mass. This is very much expected because of a deeper potential well formed by higher mass haloes.
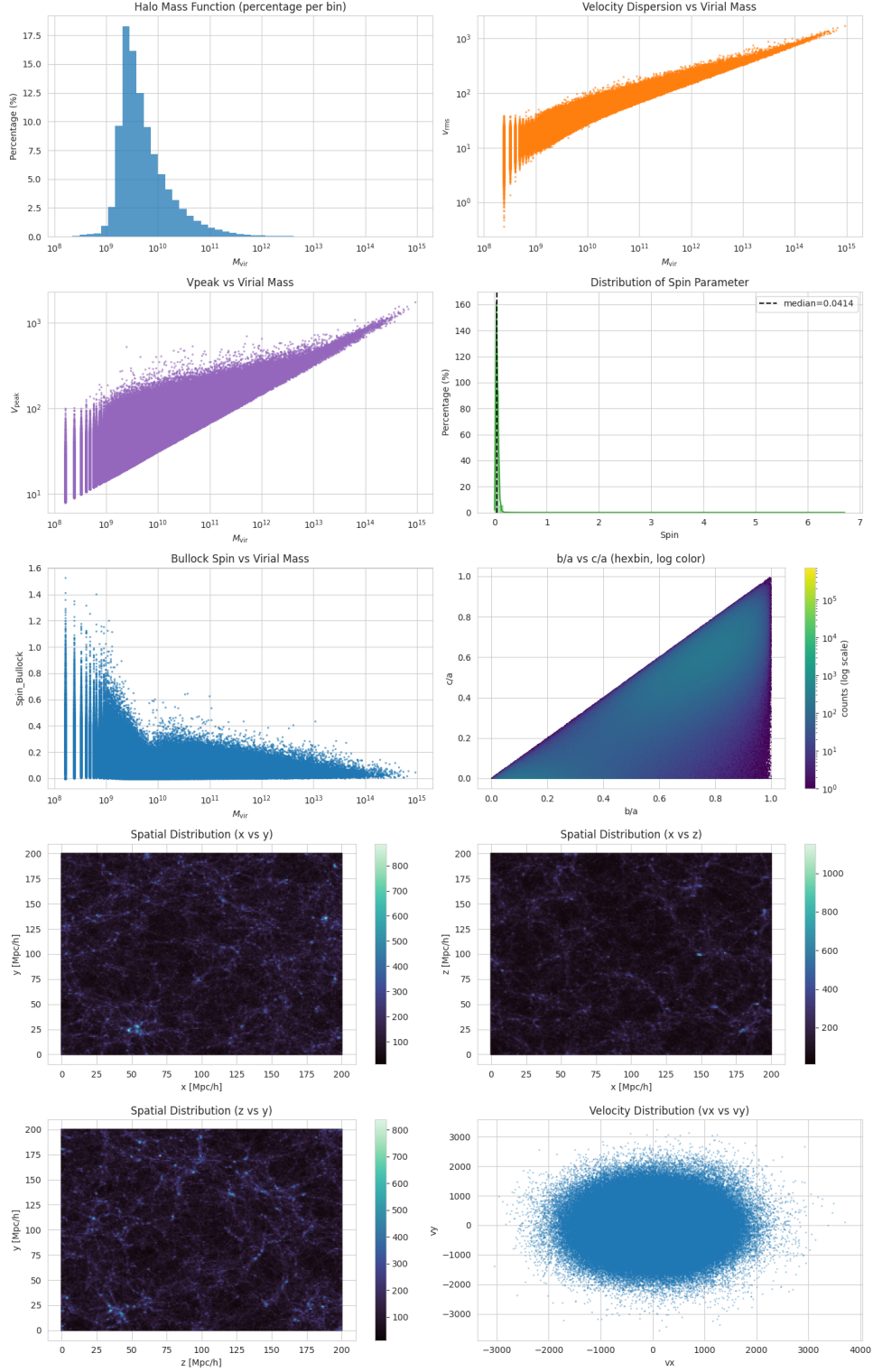
Figure 2.1

3. **Spin Parameter Distribution:** The spin parameter (λ) distribution peaks sharply at low values ($\lambda \sim 0.03$–0.05). The presence of a small high-spin tail likely corresponds to recently merged or unrelaxed halos.

4. **Spin–Mass Relation:** The Bullock spin parameter ($\lambda_{\mathrm{Bullock}}$) shows a weak inverse correlation with virial mass, indicating that low-mass halos tend to have slightly higher spins.

This behavior is consistent with the tidal torque theory, where angular momentum acquisition is more efficient for smaller systems.

5. **Shape Distribution (b/a vs. c/a):** The hexbin map of axis ratios indicates that most halos are moderately triaxial, clustering around $b/a, c/a \approx 0.4$–0.8. The triangular region arises from the geometric constraint $c/a \leq b/a \leq 1$.

6. **Spatial Distribution:** The (x, y), (x, z), and (z, y) hexbin density maps reveal a filamentary large-scale structure characteristic of the cosmic web. Dense nodes connected by filaments and surrounded by underdense voids reproduce the expected morphology of dark matter distribution $z \approx 0$.

7. **Velocity Distribution:** The velocity scatter (v_x, v_y) shows a symmetric, roughly elliptical distribution centered around zero, implying isotropic velocity dispersion and the absence of large-scale bulk flows. The Gaussian-like spread supports the interpretation that halos are statistically virialized and dynamically relaxed.

2.4 Assembly Bias trends

In this section we reproduce Fig. 1 of []. We use the measurements of the halo bias and various other internal properties obtained from the simulated data .

2.4.1 Due to tidal anisotropy (α)

We compute the tidal anisotropy at $4 \times R_{200b}$ as used in the paper. We have the eigenvalues of the tidal tensor at $4 \times R_{200b}$ in the columns: "lam1_R4R200b", "lam2_R4R200b" and "lam3_R4R200b" of vahc.csv. Using these and the usual formula for α as given in the paper and discussed in the previous section we compute the tidal anisotropy (α) for each halo. We then perform logarithmic binning for the mass range and for every bin, we sort the halos in increasing order of α and make quartiles: $Q1 = 0 - 25\%$, $Q2 = 25\% - 50\%$, $Q3 = 50\% - 75\%$ and $Q4 = 75\% - \text{rest}$ with respect to the values of α. We then obtain the quartile plot of the halo bias(b_1) vs M_{vir}, the quartiles being with respect to α. The plot is obtained as shown in the figure below:
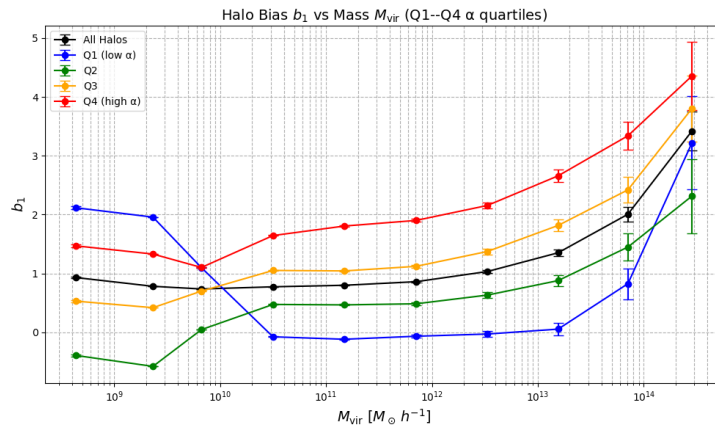

Figure 2.2: Assembly bias for α: tidal anisotropy

Inference: Out of the 10 bins (0-9) the results for bin 3-9 matches satisfactorily with the paper. There is some abnormality in the low mass range(bin: 0-2). To figure that out, we print the no. of halos per quartile per bin and also the min/max values for each such quartile for each bin. For bins 0-2, we observe that a large no. of halos get the same value of α (near zero)

and that therefore doesn't show reliable assembly bias trends in this mass range. So we can conclude that haloes in isotropic environments (small α) are substantially less clustered(low b_1) than those in anisotropic environments (high α).

2.4.2 Due to Spin

We follow the same procedure as before with the "Spin" column of the "extended.csv" data which actually is the Peebles spin parameter as discussed in the paper as well as in the previous section. We then obtain the following plot. Again the plot agrees quite well with that in Fig. 1 in the paper.

Figure 2.3: Assembly bias for λ: Peebles' Spin

Inference: We observe that the assembly bias trend is stronger for the high mass range (bins-6 7,8,9) while for lower masses (bin-0-5), the halo spin shows nearly no assembly bias. This can be explained as follows:
At early times, a halo's spin mostly comes from the tidal torques. For low mass haloes this process happens early, in relatively linear environments. Their environments are kind of isolated thus having not much connection between their spin and the large-scale environment. On the contrary, for high mass haloes, they form later through lots of mergers in denser regions. Their spin is heavily influenced by how and when they merge. Since dense regions statistically have more merger activity, spin becomes correlated with the environment thus showing high positive assembly bias. We also observe that for high mass haloes (bin 6-9), haloes with smaller spin are less clustered than those with higher spins.

2.4.3 Due to c/a

After following a similar procedure for the halo shape asphericity (c/a) using the c_to_a column of the extended.csv file, we get the following plot:
 Inference: The assembly bias trend matches with that in the paper for bins 1-8, for bin 9, there aren't enough no. of haloes, and therefore not showing reliable statistics. For bin 0, we again have same value of c/a for a large number of haloes thus not showing reliable assembly bias trend.
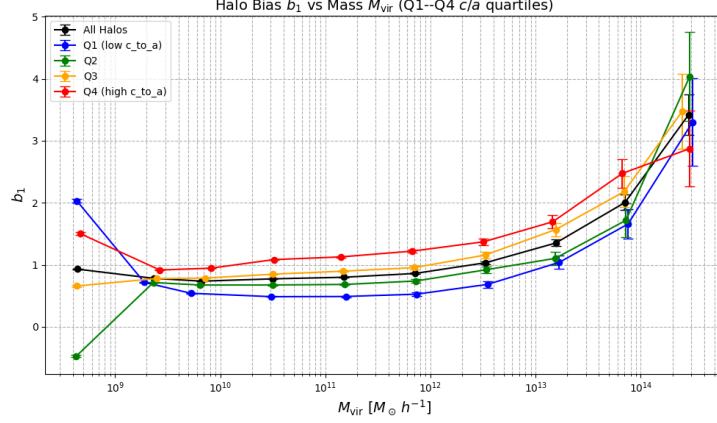
Figure 2.4: Assembly bias for c/a: Halo Shape asphericity

2.4.4 Due to c_{vir}

We compute the halo concentration(c_{vir}) for each one of the haloes and follow again the similar procedure as before to get the following quartile plot.
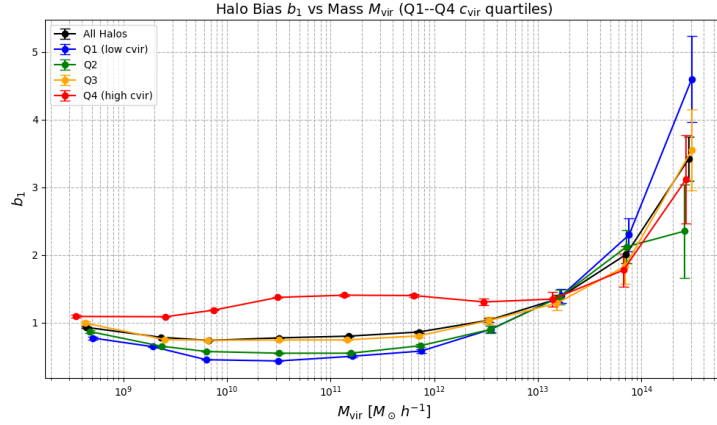

Figure 2.5: Assembly bias for c_{vir}: Halo Concentration

Inference: As similar to the paper, the assembly bias for c_{vir} shows a more complex trend. For lower masses (bins 0-7), the haloes show a positive assembly bias with respect to c_{vir}, i.e. highly concentrated haloes being more clustered. For higher masses this flips. This inversion as can be observed from the plot happens at nearly $M_{vir} \sim 10^{13} h^{-1} M_{\odot}$ and this matches with that reported in the paper.

2.5 Tidal Anisotropy as an indicator of assembly bias

To determine whether the tidal anisotropy (α) is an indicator or acts as an intermediate step for assembly bias, we use the concept of conditional correlation coefficients. We first apply a mass cut $M_{\text{vir}} > 10^{10} \ h^{-1} M_{\odot}$, since low mass haloes doesn't show significant assembly bias trends as observed in the previous section. We then split the remaining haloes into 10 logarithmically spaced mass bins. We, thereafter compute the conditional correlation coefficient:

$$\gamma_{b_1,c|\alpha} \ = \ \gamma_{b_1,c} \ - \ \gamma_{b_1,\alpha} \, \gamma_{\alpha,c}, \tag{2.9}$$

where c is some internal property. We then use the same reasoning as used in the paper that if $\gamma_{b_1,c|\alpha} = 0$, then $\gamma_{b_1,c} \ = \ \gamma_{b_1,\alpha} \, \gamma_{\alpha,c}$ which implies that the b_1-property covariance is explained

by the joint correlation of both b_1 and c with α. In other words, conditioning on α removes the assembly bias trend for the internal properties. We now try to reproduce this result using our data. In this analysis we use Spearman's rank correlation. We first compute the Spearman's rank correlation between α and an internal property(left panel), which depicts the corr. between the tidal environment and the halo internal properties, next we compute the same for b_1 and an internal property(middle panel) which depicts the assembly bias of halo internal properties and at last the conditional correlation coefficients between b_1 and the internal properties, conditioned on α, which basically depicts the residual assembly bias at fixed tidal environment.
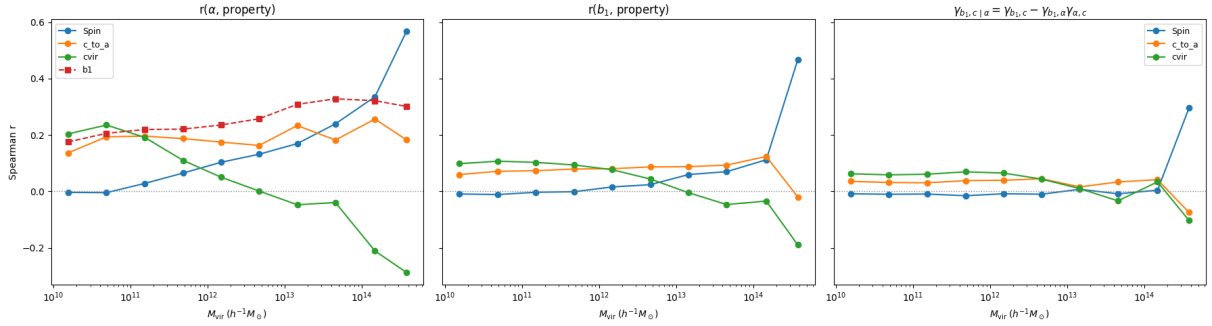

Figure 2.6: Correlations between internal halo properties, tidal environment and large scale bias

Inference: The left panel broadly matches with the paper depicting a positive correlation between the tidal environment and the clustering strength, spin and halo shape asphericity, while showing a positive correlation for lower masses and a negative correlation for higher masses with the halo concentration. The middle panel summarizes the assembly bias trends we obtained earlier. And the right panel depicts the result of the paper that the conditional correlation coefficients (although not 0) significantly reduce in magnitude from the unconditional coefficients in the middle panel (only large residuals remain for higher mass haloes). This suggests that conditioning on the tidal anisotropy α largely accounts for the assembly bias trend of the internal halo properties, thus producing the main result of the paper.

Spin-Tidal tensor correlations

Our goal is to predict the spin-direction using the tidal tensor components.

Let's first do it the wrong way: we try to find correlations between the tidal tensor components and the normalized angular momentum components- $\hat{j}_x, \hat{j}_y, \hat{j}_z$: This is very obviously

```
Correlation Matrix: All Spin Components vs All Tidal Tensor Components
        tens11_R4R200b  tens22_R4R200b  tens33_R4R200b  tens12_R4R200b  \
jx_u          0.000544        0.000699        0.000651        0.000562
jy_u          0.000266        0.000060        0.000021       -0.000191
jz_u          0.000256        0.000718        0.000807       -0.000202

        tens13_R4R200b  tens23_R4R200b
jx_u         -0.000073        0.000365
jy_u         -0.000285        0.000650
jz_u          0.000025        0.000673
```

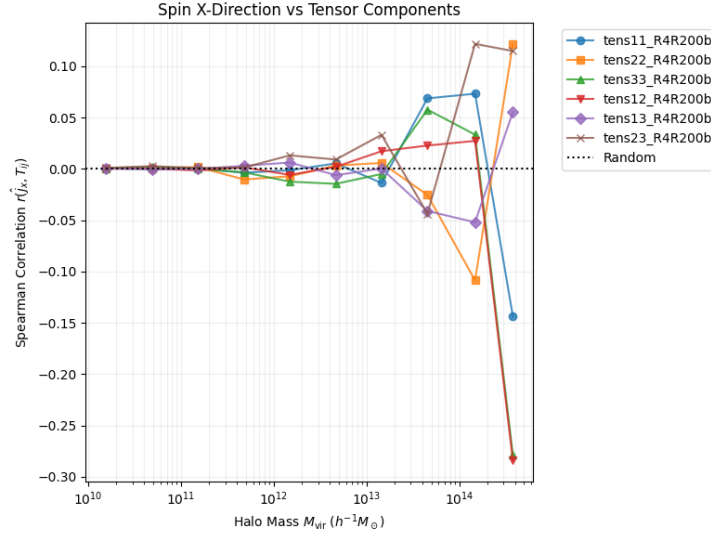Figure 3.1: Correlation matrix between $\hat{j}_i$ and T_{ij}

Figure 3.2: Mass-binned correlations between T_{ij} and $\hat{j}_x$

wrong. And also from the plots and the correlation matrix, we can confirm that there is near zero correlation (or noise) between the tidal tensor components and the normalized angular-momentum components. This must be obvious due to the following reason: the tidal tensor components and the angular momentum components we obtain from the simulation data are in the simulation box co-ordinates which are arbitrary. Rotating the box frame would change the correlations. The mass-binned correlations we obtain are near zero, which is expected due to isotropy. Large fluctuations at high mass is due to small-number statistics. We should then rather switch to the eigen-frame, by (say) taking projections of the normalised angular momentum in the eigen-basis ($|\hat{j} \cdot \vec{e}_i|$). Here, $\vec{e}_1$, $\vec{e}_2$ and $\vec{e}_3$ are the eigen vectors corresponding to the eigen values $\lambda_1 < \lambda_2 < \lambda_3$. Since the tidal tensor describes the curvature of the gravitational potential, a larger positive eigenvalue corresponds to stronger tidal compression. Therefore, $\vec{e}_3$, corresponding to the maximum eigenvalue (λ_3), represents the direction of strongest collapse. Conversely, $\vec{e}_1$, associated with the minimum eigenvalue (λ_1), defines the direction of slowest collapse (or expansion). Because matter is not being crushed along this direction, it's termed as the filament axis. $\vec{e}_2$ naturally defines the intermediate axis, orthogonal to the other two.

At first, we take all the haloes in our data, for each, we compute the eigen vectors and compute the projections. We do this for all different scales. We create mass bins and compute averages of the projections in each bin and obtain the following plots: What we see above is
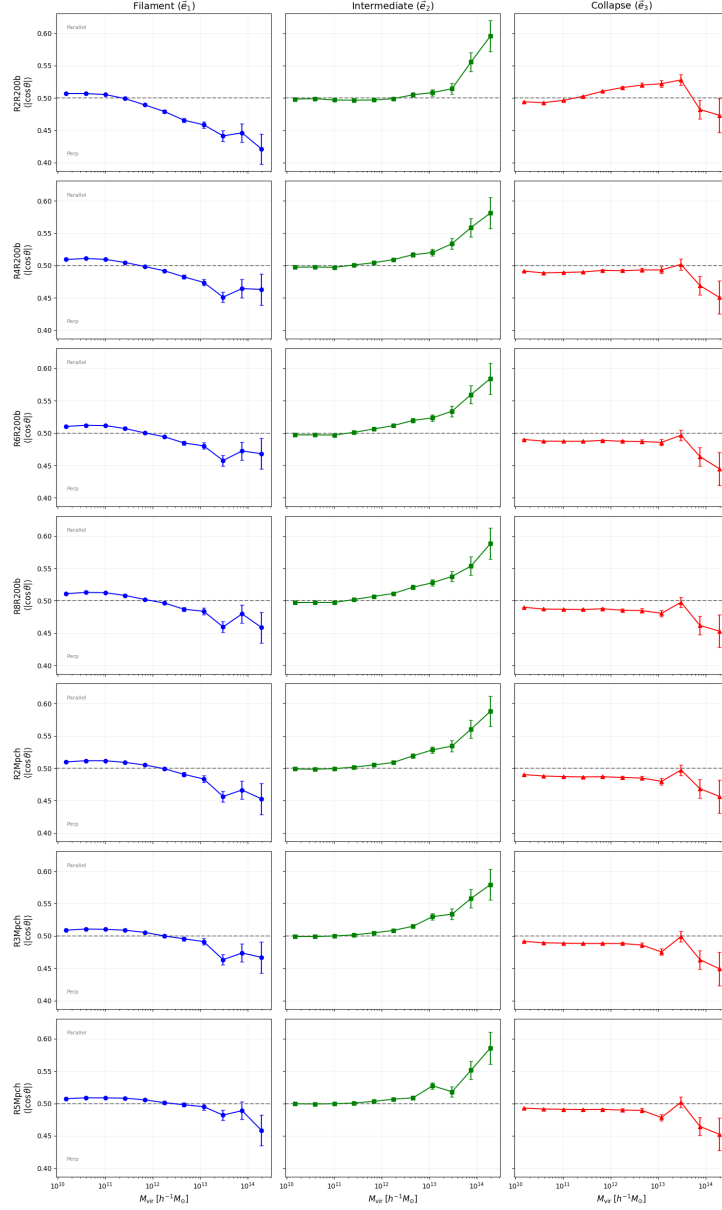

Figure 3.3: Mass-dependent spin alignment for halos across multiple smoothing scales. Curves show the mean absolute dot product $\langle |\hat{j} \cdot \vec{e}_i| \rangle$ for the filament $(\vec{e}_1)$, intermediate $(\vec{e}_2)$, and collapse $(\vec{e}_3)$ axes. The horizontal dashed line at 0.5 indicates the expectation for a random isotropic distribution.

known as the spin-flip phenomenon. In these plots, the horizontal line at 0.5 marks the baseline for a random, isotropic distribution. We observe distinct, mass-dependent behaviors for the projections along each eigen-vector:

- The Filament Axis $(\mu_1 = |\hat{j} \cdot \vec{e}_1|)$: At low masses, the signal is slightly above 0.5, indicating that small haloes tend to align their spins parallel to the axis of slowest collapse $(\vec{e}_1)$. However, as we move to higher masses, the curve crosses 0.5 and drops below it. This confirms that high-mass haloes preferentially orient their spins perpendicular to $\vec{e}_1$.

- The Collapse Axis $(\mu_3 = |\hat{j} \cdot \vec{e}_3|)$: The trend for μ_3 is relatively flat and stays near or

14

slightly below 0.5 across the entire mass range. This tells us that halo spins generally avoid aligning with the direction of fastest collapse ($\vec{e}_3$). This makes physical sense: it is difficult for a halo to rotate along the same direction that the environment is crushing it.

- The Intermediate Axis ($\mu_2 = |\hat{j} \cdot \vec{e}_2|$): The μ_2 component essentially acts as the "receiver" of the spin flip. At low masses, it hovers near the random baseline. But at high masses-exactly where μ_1 drops, μ_2 rises significantly above 0.5. This suggests that as massive haloes flip away from $\vec{e}_1$ while continuing to avoid $\vec{e}_3$, their spins settle into alignment with the intermediate axis ($\vec{e}_2$).

This transition points to a fundamental change in the mechanism driving halo growth. The prevailing physical picture is that low-mass haloes acquire angular momentum through "winding" accretion flows along the filament (parallel alignment) [6]. High-mass haloes, on the other hand, grow primarily through major mergers traveling down the filament axis. These mergers generate orbital angular momentum perpendicular to the direction of motion, resulting in the perpendicular alignment we observe [6].

However, "all haloes" mixes distinct environments. We need to verify if this "spin-flip" is a universal feature or if it is driven by specific geometries. To do this, we classify each halo into its respective web environment: Void, Sheet, Filament, or Knot. Since a positive eigenvalue implies collapse (compression) along that axis, and a negative eigenvalue implies expansion, we define the environments by the number of collapsing axes [4]:

- Voids: Expanding in all three directions ($\lambda_3 < 0$).

- Sheets: Collapsing along one axis ($\lambda_3 > 0$ and $\lambda_2 < 0$) while expanding along the other two. This forms a planar structure.

- Filaments: Collapsing along two axes ($\lambda_2 > 0$ and $\lambda_1 < 0$). This forms a cylindrical tube.

- Knots: Collapsing in all three directions ($\lambda_1 > 0$). These are high-density peaks like galaxy clusters.

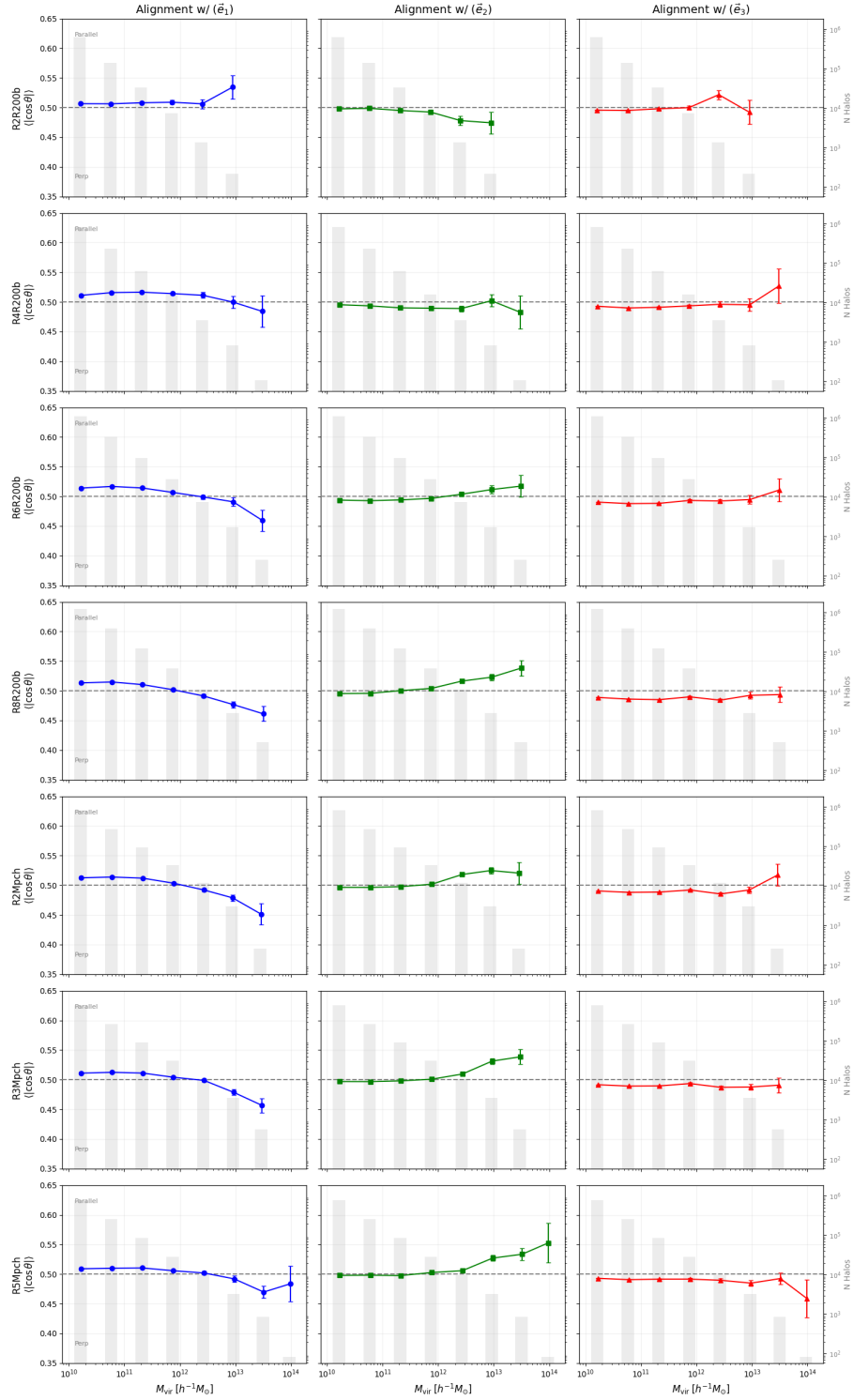We then repeat the eigen-frame analysis for each environment separately.

Figure 3.4: Mass-dependent spin alignment for halos in the filament environments across multiple smoothing scales. Curves show the mean absolute dot product $\langle |\hat{j} \cdot \vec{e}_i| \rangle$ for the filament ($\vec{e}_1$), intermediate ($\vec{e}_2$), and collapse ($\vec{e}_3$) axes. The horizontal dashed line at 0.5 indicates the expectation for a random isotropic distribution. Background histograms represent the halo count (N) in each mass bin.
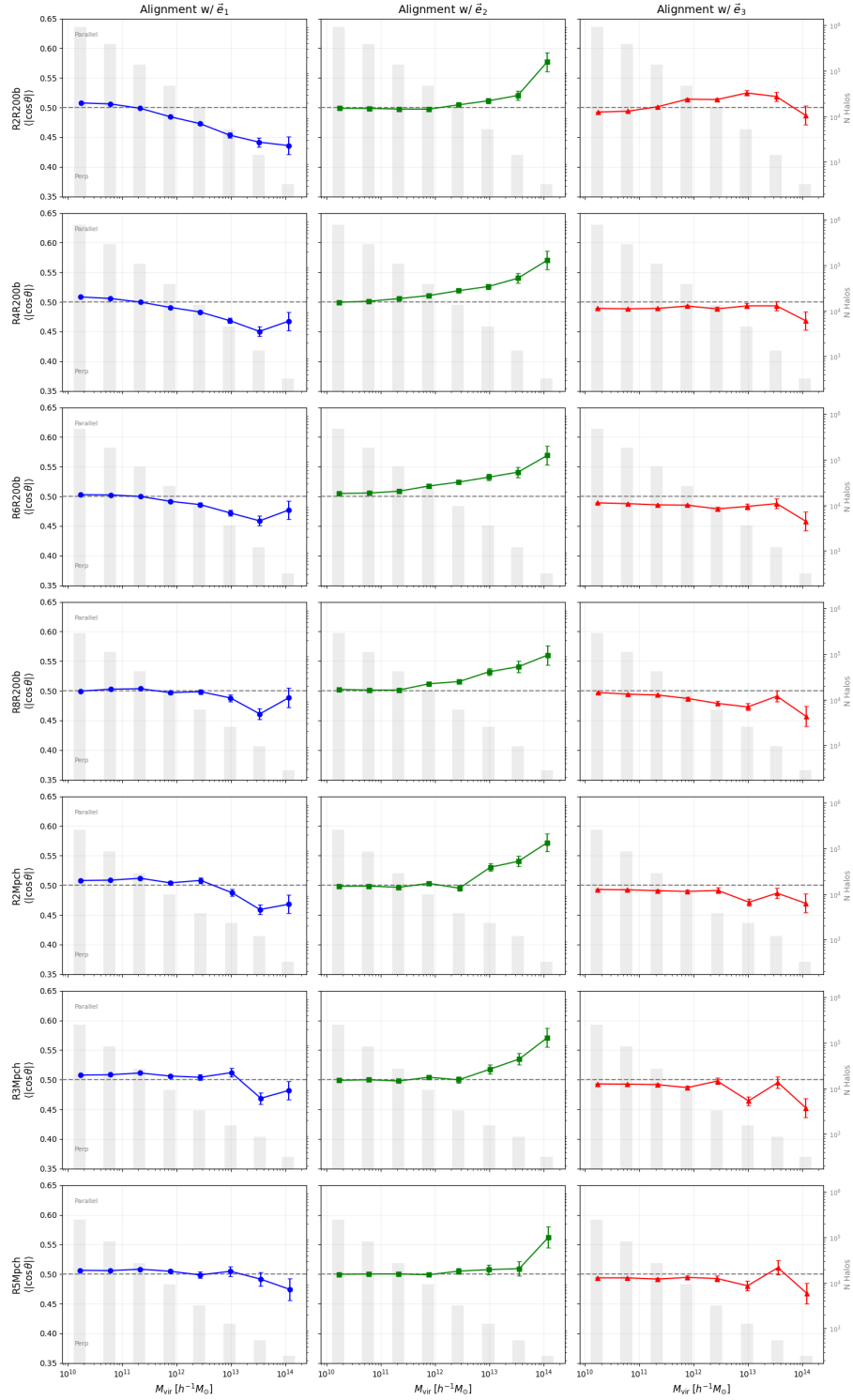
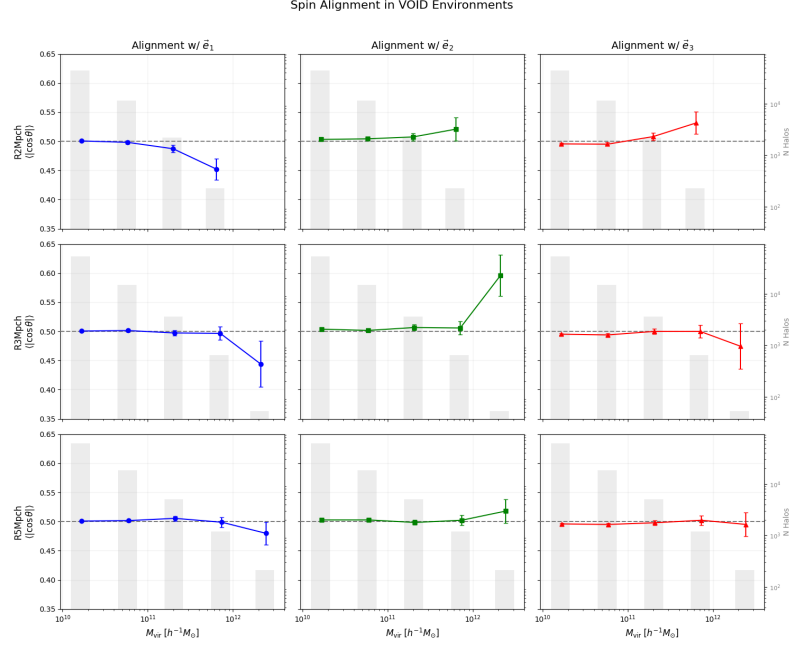Figure 3.5: Same as 3.4 but for knot environments

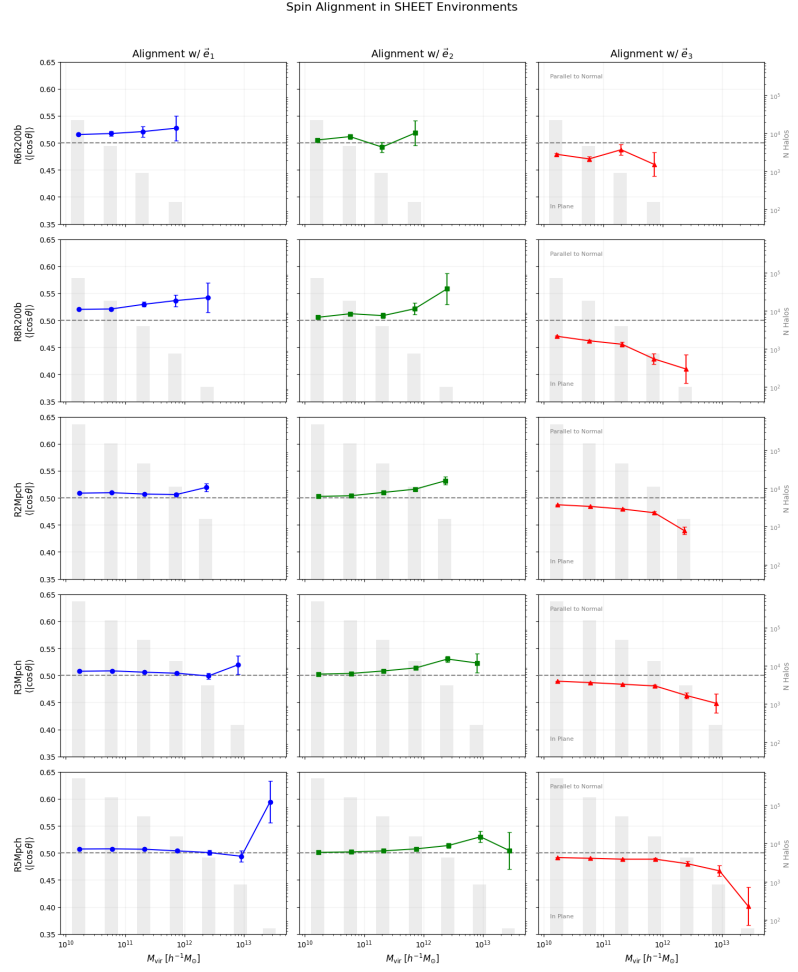Figure 3.6: Same as 3.4 but for void environments

Figure 3.7: Same as 3.4 but for sheet environments

3.0.1 Some Observations

In both knot and filament environments, a transition is observed in the alignment with the filament axis (μ_1). Low-mass halos align parallel to the axis ($\mu_1 > 0.5$), while high-mass halos align perpendicular to it ($\mu_1 < 0.5$) with the spin flip occurring at around $M_{tr} \sim 10^{12}h^{-1}M_\odot$ for filaments and around $M_{tr} \sim 10^{11}h^{-1}M_\odot$ for knots. As the parallel alignment (μ_1) drops for high-mass halos, the alignment with the intermediate axis (μ_2) typically rises. This indicates that the spin is flipping into the plane perpendicular to the filament axis. However, the trends depend very much on the smoothing scale. For filaments, the alignment signal for μ_1 becomes stronger at larger smoothing scales. This confirms that the tidal tensor at these scales captures the long-range geometry of the filament, which drives the accretion flow. For filaments, we also observe an increase in halo counts at larger scales. This is because massive halos, which appear as isolated knots when smoothed locally, appear as dense nodes embedded within large-scale filaments when smoothed over larger scales. Unlike filaments, we see that the alignment signal in knots is strongest at small scales and washes out at large smoothing scales. For sheet environments though, the alignment μ_3 is consistently low, indicating that halo spins are confined to lie within the plane of the sheet ($\vec{e}_1$-$\vec{e}_2$ plane). Matter collapses onto the sheet along $\vec{e}_3$ but flows within the sheet plane. Tidal torques are most effective within the plane of flow, making it dynamically difficult to generate rotation around the axis of compression. Voids exhibit the weakest alignment signals of all environments. The void population is dominated almost entirely by low-mass dwarfs, with virtually no massive haloes ($M > 10^{13}h^{-1}M_\odot$). Since Voids are expanding in all three directions ($\lambda_1, \lambda_2, \lambda_3 < 0$), there is no strong collapse axis to organize the rotation. The resulting weak tidal field leads to spin orientations that are largely consistent with random isotropy.

The observations seem to agree with that reported in [4], [3] or [5]

Bibliography

[1] Sujatha, et al., *Cosmic web anisotropy is the primary indicator of halo assembly bias*, https://arxiv.org/abs/1903.02007 (2019).

[2] Porciani, et al., *Testing tidal-torque theory – I. Spin amplitude and direction*, https://doi.org/10.1046/j.1365-8711.2002.05305.x (2002).

[3] Wang, P. and Kang, X., *A general explanation on the correlation of dark matter halo spin with the large-scale environment*, MNRAS Letters, 468, 1, L123–L127, https://doi.org/10.1093/mnrasl/slx038 (2017).

[4] Hahn, O., Porciani, C., Carollo, C. M., and Dekel, A., *Properties of dark matter haloes in clusters, filaments, sheets and voids*, MNRAS, 375, 489–499, https://arxiv.org/abs/astro-ph/0610280 (2007).

[5] Aragón-Calvo, M. A., van de Weygaert, R., Jones, B. J. T., and van der Hulst, J. M., *Spin Alignment of Dark Matter Halos in Filaments and Walls*, The Astrophysical Journal Letters, 655, L5, https://arxiv.org/abs/astro-ph/0610249 (2007).

[6] Codis, S., Pichon, C., Devriendt, J., et al., *Connecting the cosmic web to the spin of dark haloes: implications for galaxy formation*, MNRAS, 427, 4, 3320–3336, https://doi.org/10.1111/j.1365-2966.2012.21636.x (2012).